

## How Solid-Electrolyte Interphase Forms in Aqueous Electrolytes

Liumin Suo,<sup>†</sup> Dahyun Oh,<sup>‡,§</sup> Yuxiao Lin,<sup>||</sup> Zengqing Zhuo,<sup>⊥,#</sup> Oleg Borodin,<sup>¶</sup> Tao Gao,<sup>∇</sup> Fei Wang,<sup>¶,∇</sup> Akihiro Kushima,<sup>⊗</sup> Ziqiang Wang,<sup>⊗</sup> Ho-Cheol Kim,<sup>§</sup> Yue Qi,<sup>||</sup> Wanli Yang,<sup>⊥</sup> Feng Pan,<sup>#</sup> Ju Li,<sup>\*,¶,⊗</sup> Kang Xu,<sup>\*,¶</sup> and Chunsheng Wang<sup>\*,∇,||</sup>

<sup>†</sup>Key Laboratory for Renewable Energy, Beijing Key Laboratory for New Energy Materials and Devices, Beijing National Laboratory for Condensed Matter Physics, Institute of Physics, Beijing 100190, China

<sup>‡</sup>Biomedical, Chemical and Materials Engineering Department, San José State University, San Jose, California 95112, United States

<sup>§</sup>IBM Almaden Research Center, San Jose, California 95120, United States

<sup>||</sup>Department of Chemical Engineering and Materials Science, Michigan State University, East Lansing, Michigan 48824, United States

<sup>⊥</sup>Advanced Light Source Lawrence Berkeley National Laboratory, Berkeley, California 94720, United States

<sup>#</sup>School of Advanced Materials, Peking University, Peking University Shenzhen Graduate School, Shenzhen 518055, China

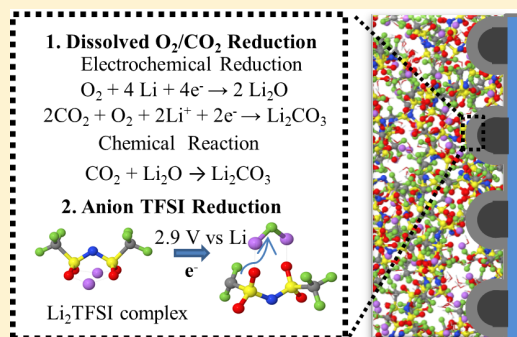
<sup>¶</sup>Electrochemistry Branch, Sensor and Electron Devices Directorate, U.S. Army Research Laboratory, Adelphi, Maryland 20783, United States

<sup>∇</sup>Department of Chemical and Biomolecular Engineering, University of Maryland, College Park, Maryland 20742, United States

<sup>⊗</sup>Department of Nuclear Science and Engineering, Department of Materials Science and Engineering, Massachusetts Institute of Technology, Cambridge, Massachusetts 02139, United States

### Supporting Information

**ABSTRACT:** Solid-electrolyte interphase (SEI) is the key component that enables all advanced electrochemical devices, the best representative of which is Li-ion battery (LIB). It kinetically stabilizes electrolytes at potentials far beyond their thermodynamic stability limits, so that cell reactions could proceed reversibly. Its ad hoc chemistry and formation mechanism has been a topic under intensive investigation since the first commercialization of LIB 25 years ago. Traditionally SEI can only be formed in nonaqueous electrolytes. However, recent efforts successfully transplanted this concept into aqueous media, leading to significant expansion in the electrochemical stability window of aqueous electrolytes from 1.23 V to beyond 4.0 V. This not only made it possible to construct a series of high voltage/energy density aqueous LIBs with unprecedented safety, but also brought high flexibility and even “open configurations” that have been hitherto unavailable for any LIB chemistries. While this new class of aqueous electrolytes has been successfully demonstrated to support diversified battery chemistries, the chemistry and formation mechanism of the key component, an aqueous SEI, has remained virtually unknown. In this work, combining various spectroscopic, electrochemical and computational techniques, we rigorously examined this new interphase, and comprehensively characterized its chemical composition, microstructure and stability in battery environment. A dynamic picture obtained reveals how a dense and protective interphase forms on anode surface under competitive decompositions of salt anion, dissolved ambient gases and water molecule. By establishing basic laws governing the successful formation of an aqueous SEI, the in-depth understanding presented in this work will assist the efforts in tailor-designing better interphases that enable more energetic chemistries operating farther away from equilibria in aqueous media.



## INTRODUCTION

Electrolytes in electrochemical devices provide an ionic pathway between anode and cathode. In advanced batteries, electrodes are often pushed to work at extreme potentials in order to maximize the energy output. These potentials situate far beyond the thermodynamic stability limits of electrolyte components (salt ions, solvent molecules), hence irreversible decomposition reactions occur. In certain (but not all) scenarios, such decompositions produce dense solid products,

which deposit on electrode surfaces, preventing sustained electrolyte decomposition while still allowing electrochemical reactions to proceed. Such an independent passivation phase is named solid-electrolyte interphase (SEI) after its electrolyte nature, i.e., insulating to long-range electron transport but conductive to ions of significance to the cell reactions. Li-ion

Received: October 6, 2017

Published: November 29, 2017

battery (LIB) chemistry owes its excellent reversibility to SEI existence on graphitic anodes, where  $\text{Li}^+$ -intercalation occurs at  $\sim 0.10$  V vs Li, far below the reduction potentials of most electrolyte solvents.<sup>1,2</sup> Emerging battery chemistries beyond Li-ion are expected to heavily rely on the ability to tailor-design and manipulate SEIs on new electrode materials.<sup>3</sup>

Thanks to the commercial success of Li-ion batteries, intensive investigations have been conducted in the past two decades on SEI formed in carbonate-based nonaqueous electrolytes. Significant knowledge has been achieved regarding the chemistry,<sup>4</sup> morphology<sup>5</sup> and formation mechanism<sup>4,6</sup> of these carbonate-originated SEIs, while various approaches have become available to tailor their properties based on the understanding of their chemical composition and morphology.<sup>7</sup> However, mysteries still exist, and debate arise often, because of the nanoscale presence and the ad hoc formation nature of SEI, and the sensitivity to ambient contaminants.

On the other hand, SEI has always been associated only with nonaqueous electrolytes, because none of the decomposition products from water, i.e.,  $\text{H}_2$  and hydroxide at anode or  $\text{O}_2$  and  $\text{H}^+$  at cathode, could deposit in solid state on electrode surfaces and form a protective interphase. This general consensus was overturned by the recent groundbreaking work of Suo et al, who successfully managed to form the very first aqueous SEI by altering  $\text{Li}^+$ -solvation sheath structure with superconcentration.<sup>8</sup> The expanded electrochemical stability window of the so-called “water-in-salt” electrolyte (WiSE), along with its later variations, enabled a series of high voltage/high energy density aqueous battery chemistries that deliver energy densities and cycling stability approaching the state-of-the-art LIB based on nonaqueous electrolytes, but without the safety concern of the latter,<sup>9–13</sup> Furthermore, the ambient-insensitivity of the aqueous nature also brought unprecedented flexibility to the form-factor of LIBs, making a cell of “open configuration” possible for the first time.<sup>14</sup>

In this work, combining various *in situ/operando* techniques and molecular dynamics (MD) simulations, we rigorously examine this new interphase that could induce transformational advance in battery materials and technology. The in-depth investigation establishes a few key guiding principles to improve the chemical durability of aqueous SEIs for future high voltage aqueous electrochemical devices.

## RESULTS AND DISCUSSION

**1. Live-Formation of Aqueous SEI.** At pH = 7, the cathodic stability limit of water locates at 2.626 V, below which water molecule starts to decompose reductively, evolving  $\text{H}_2$  and  $\text{OH}^-$ . Theoretically this reaction sets the lowest limit for an anode material to operate in dilute aqueous electrolytes. In aqueous electrochemistry, a common practice to manipulate this lowest cathodic limit is to suppress the activity of proton by adjusting the pH-value of aqueous solutions.<sup>14</sup> However, even in the strongly alkaline electrolyte (pH = 14), hydrogen evolution still occurs at 2.213 V vs Li, which is too high to accommodate most of the anode materials desired by battery scientists. Besides, a downshift of  $\text{O}_2$  evolution potential would occur simultaneously with increasing pH, keeping the gap between the anodic and cathodic limits constant at 1.23 V. This gap, known as the electrochemical stability window of aqueous electrolytes under thermodynamic equilibria, is defined by Pourbaix diagram. The slightly higher voltage of 1.5 V realized in existing aqueous battery chemistries<sup>15,16</sup> was the result of “kinetic overpotentials” of  $\text{H}_2$  or  $\text{O}_2$  evolutions,

which depends on salt concentration, catalytic activity of the electrodes and applied currents. This slight kinetic expansion is only effective when the devices are tested at high rates, otherwise parasitic reactions ( $\text{H}_2$  evolution at anode in particular) would become pronounced enough to compete with the cell reactions, significantly decimating the Coulombic efficiencies of the latter. Hence, a voltage window expansion would only be meaningful for the battery applications with the formation of an interphasial barrier, similar to SEI in LIB.

In order for such an aqueous SEI to form, its precursor must meet one primary prerequisite, i.e., its reductive decomposition has to occur at a potential before major water decomposition occurs, so that interference from the competitive  $\text{H}_2$  evolution could be minimized. In the seminal work of Suo et al.,<sup>8</sup> this was achieved by superconcentration (21 m) of LiTFSI, where the altered  $\text{Li}^+$ -solvation sheath structure promotes the reduction of anion TFSI from 1.40 V to a higher range (2.30–2.90 V depending on the reaction pathways), thus making it possible to form a dense and protective interphase based on LiF. Since this range significantly overlaps with the  $\text{H}_2$  evolution potential ( $\sim 2.60$  V, at pH = 6.8 for LiTFSI/ $\text{H}_2\text{O}$ ), at least part of the irreversible capacity observed during the first charging should be contributed by the water decomposition, along with the reduction of TFSI. Figure 1a,b,c,d showed voltage profiles of the aqueous Li-ion full cells based on  $\text{LiMn}_2\text{O}_4$  cathode and Chevrel-phase  $\text{Mo}_6\text{S}_8$  anode in aqueous electrolytes at four different LiTFSI concentrations (1 m, 5 m, 10 and 21 m). Both these electrodes are intercalation-type materials known for their excellent rate capabilities. The irreversible capacities, defined as the difference between the charge and discharge capacities in the first full cycle, showed strong dependence on salt concentration. Since both  $\text{Mo}_6\text{S}_8$  anode and  $\text{LiMn}_2\text{O}_4$  cathode have two characteristic  $\text{Li}^+$ -intercalation plateaus ( $\sim 2.2$  V/ $\sim 2.5$  V and  $\sim 4.1$  V/ $\sim 4.3$  V vs Li, respectively, depending on salt concentrations), ideally the full cell voltage should consist of two corresponding plateaus at  $\sim 1.5$  V and  $\sim 2.1$  V. As described previously, however, the higher plateau (which corresponds to full lithiation of  $\text{Mo}_6\text{S}_8$  anode at 2.20 V vs Li) cannot be accessed by diluted aqueous electrolytes due to extensive water decomposition, as indicated by the long flat  $\text{H}_2\text{O}$  decomposition plateau above 1.80 V (Figure 1a). As salt concentration increases, this upper flat plateau gradually shifted up (Figure 1b and 1c), accompanied by rapid decrease in the irreversible capacity (Figure S1). Meanwhile, the second  $\text{Li}^+$ -intercalation plateau at  $\sim 2.0$  V appears, until at 21 m (Figure 1d), where the columbic efficiency reached 86%, with only  $\sim 7.7$  mAh/g out of 43 mAh/g overall capacity is irreversible. This irreversible part is believed to be mostly attributed to the SEI formation due to the reduction of TFSI and dissolving gases ( $\text{CO}_2$  and  $\text{O}_2$ ) reductions.

To quantitatively study this formation chemistry, an *in situ* electrochemical analysis technique, i.e., differential electrochemical mass spectrometry (DEMS),<sup>17</sup> was used to monitor the gaseous compounds during the initial charging process and how they change with the salt concentration. Figure 1e,f,g,h display the DEMS collected from the identical aqueous full Li-ion cells. As expected, in diluted solution (1 m), the water splitting overwhelmed the irreversible process, cumulatively producing 84117 nmol  $\text{H}_2$  and 22438 nmol  $\text{O}_2$  continuously when the cell is charged above 1.8 V (Figure 1e). It should be noted here that the amounts of  $\text{H}_2$  and  $\text{O}_2$  do not precisely obey the 2:1 stoichiometric ratio, revealing that the irreversible

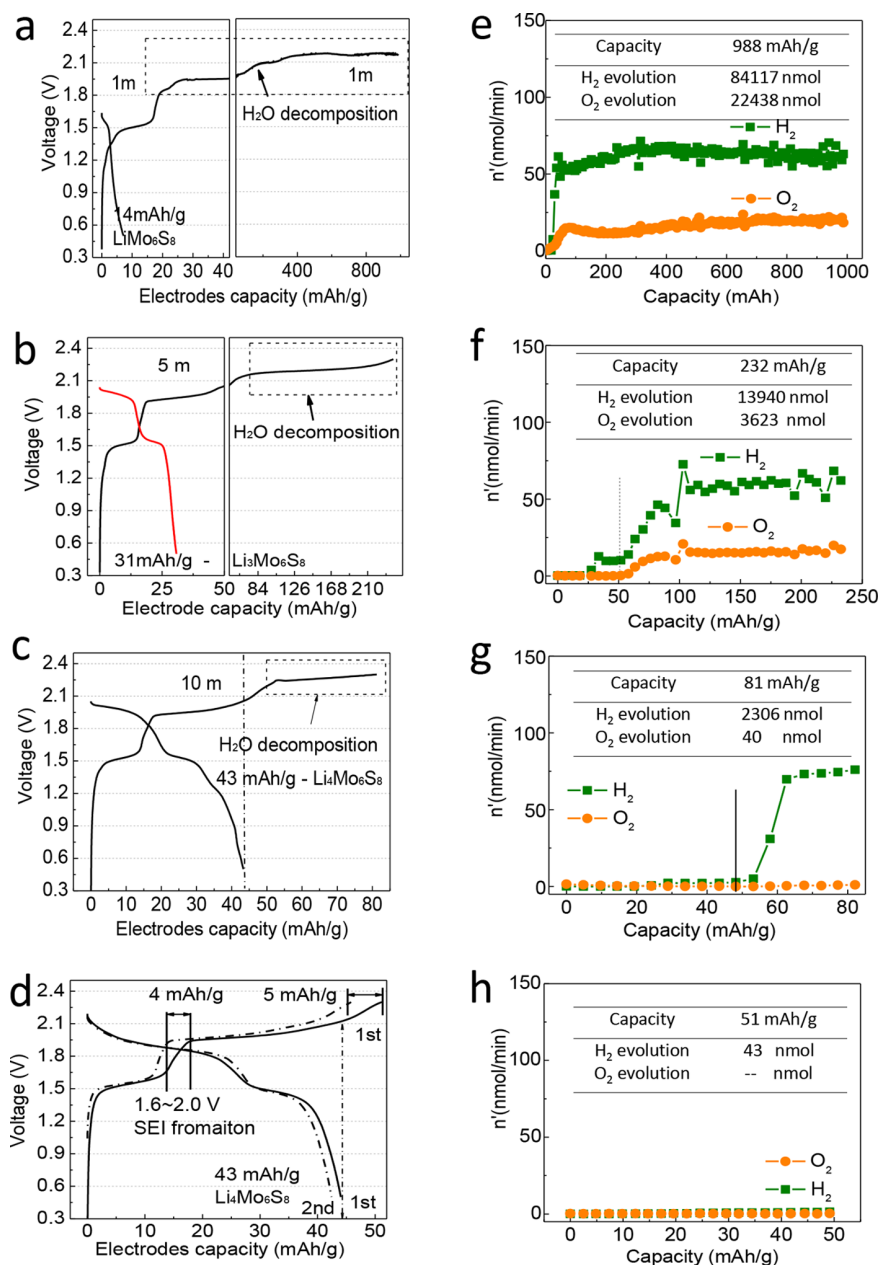


**Figure 1.** (a–d) Voltage profiles for the first charge–discharge profiles of full Li-ion cells constructed with Mo<sub>6</sub>S<sub>8</sub> anode and LiMn<sub>2</sub>O<sub>4</sub> cathode and cycled in four aqueous electrolytes of different salt concentrations. In these full cell configurations the anode and cathode are coupled at LiMn<sub>2</sub>O<sub>4</sub>/Mo<sub>6</sub>S<sub>8</sub> = 2:1 by weight. (e–h) H<sub>2</sub> and O<sub>2</sub> evolution monitored during the first charging process using differential electrochemical mass spectrometry (DEMS) in these same aqueous full Li-ion cells.

process, even in the diluted electrolyte, is not entirely corresponding to water splitting, while other competing processes such as Li<sup>+</sup>-intercalation and anion reduction also exist simultaneously. With increasing LiTFSI concentration, the water decomposition at cathode surface is apparently suppressed by much higher extent than at anode surface, as O<sub>2</sub> almost completely disappears at 10 m, while H<sub>2</sub> continues to generate until 21 m (Figure 1g and 1h). This distinction is consistent with the general knowledge that the kinetics of H<sub>2</sub> evolution is much facile than O<sub>2</sub> evolution, and serves as a strong rationale for the so-called “cathodic challenge”,<sup>13,18</sup> i.e., that the most severe challenge for high voltage aqueous batteries comes from the stabilization of anode rather than

cathode surface. At 21 m (the “water-in-salt” electrolyte, or WiSE), the O<sub>2</sub> evolution is completely eliminated during the first charging process, while negligible amount (43 nmol) of H<sub>2</sub> is still detected (Figure 1h), corresponding to ~0.00115 mAh/g irreversible capacity. In other words, in the overall irreversible capacity obtained in WiSE during the first cycle (~5 mAh/g), only ~0.02% is contributed by the water reduction, while, reductions of other species including TFSI account for the majority of the irreversible process. Although this percentage distribution could be overestimated in favor of TFSI due to the delayed diffusion of H<sub>2</sub> across electrolyte and to mass spectrometer, qualitatively it still shows how much superconcentration has promoted TFSI-reduction in its

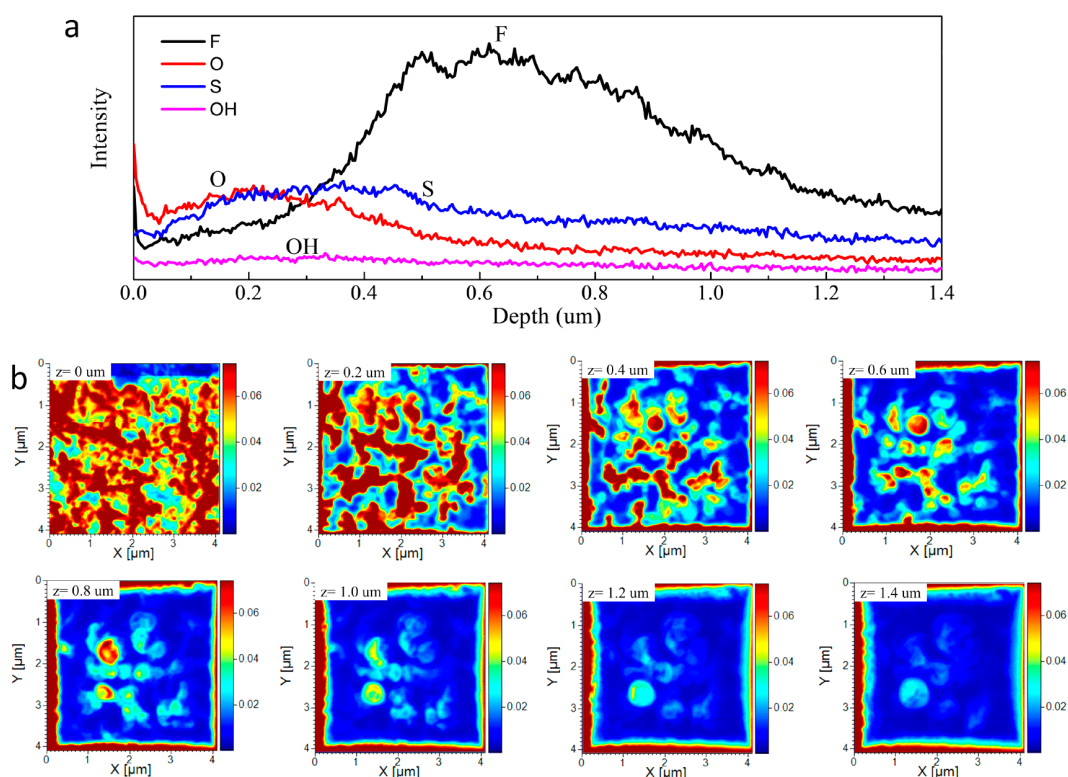


**Figure 2.** Time-of-flight secondary ion mass spectrometry (TOF-SIMS) analysis of cycled  $\text{Mo}_6\text{S}_8$  electrode after being cycled for 40 times at 0.5 C (Negative mode). (a) TOF-SIMS depth-profiles of various chemical species, and (b) the variation of SIMS total intensity with the etching depth.

competition with water decomposition. It was this preferential reduction of salt anion that is responsible for the opportunity of forming an SEI in an aqueous media. Examining the voltage profile and capacity for the second cycle (Figure 1d), one could visually conclude that this irreversible process essentially disappears. However, as the Coulombic efficiency indicates, trace amount of water decomposition persists (Figure 1h), until SEI is perfected in at least a few more cycles following the very first charging process.<sup>8</sup>

The chemical composition and distribution of SEI throughout the 3D-porous electrode is further investigated using time-of-flight secondary ion mass spectrometry (TOF-SIMS) in both negative and positive modes (Figure 2, Figure S2–S4). Ga-ion sputtering generate five negative species (Figure S3), including  $\text{F}^-$  ( $m/e = 19$ ),  $\text{S}^-$  ( $m/e = 32$ ),  $\text{O}^{2-}$  ( $m/e = 16$ ), and  $\text{OH}^-$  ( $m/e = 17$ ), with  $\text{F}^-$  being the dominant. This is consistent with our earlier conclusion that LiF exist as the main SEI component on the cycled anode surface, as revealed by X-ray photoelectron spectroscopy (XPS) and Energy-dispersive X-ray spectroscopy (EDX).<sup>8</sup> The presence of O-containing species, previously not revealed by XPS, implies that ingredients other than LiF also exist in this aqueous SEI.

In order to eliminate the possible interferences from poly(tetrafluoroethylene) (PTFE) binder and carbon black conductive additive in the composite anode, the positive mode of TOF-SIMS was also measured under the same condition, which detects positive cluster species ( $\text{Li}_2\text{F}^+$  ( $m/e = 33$ ) beside naked  $\text{Li}^+$  (Figure S4). Assuming that  $\text{F}^-$  in negative mode comes from PTFE, then  $\text{C}^+$  ( $m/e = 12$ ) and related C–F fragments ( $\text{CF}^+$   $m/e = 31$ ,  $\text{CF}_2^+$   $m/e = 50$ ,  $\text{CF}_3^+$   $m/e = 69$ ) should also be detected in positive mode.<sup>19,20</sup> In fact, their absence confirms that the dominant  $\text{F}^-$  comes from LiF in the

SEI. The depth-profiles of SEI was established by etching a selected area on the electrode surface, which was subject to continuous Ga-ion sputtering (Figure 2). The LiF-based interphasial species was revealed to penetrate the anode surface (Figure 2a), whose intensity reaches a maximum at 600–800 nm followed by gradual decay. It should be cautioned here that this maximum depth should not be mistaken as SEI thickness, considering that the electrode surface is highly porous; rather, it reflects the distribution of SEI species throughout the microstructure of the porous electrode.

In view of the possibilities of minor interphasial species other than LiF, two additional surface-sensitive techniques, XPS (Figure 3a–f) and soft-X-ray absorption spectra (sXAS) (Figure 3g–i), were also used to provide a more comprehensive chemical picture. The former, aimed to describe qualitatively the SEI components and its space distribution, was conducted with  $\text{Ar}^+$ -sputtering at different intervals, while the latter, with the purpose to relate SEI chemical composition to relative potential, was carried out on  $\text{Mo}_6\text{S}_8$  at different states-of-charge (SOC) of 1.4, 1.6, 1.9, 2.0 and 2.3 V, respectively. In both experiments,  $\text{Mo}_6\text{S}_8$  electrodes were recovered from cycled cells at designated potentials. Both XPS and SXAS revealed the presence of  $\text{Li}_2\text{CO}_3$  and  $\text{Li}_2\text{O}$  on the surface of cycled electrode (Figure 3), which revised our previous understanding of the aqueous SEI formed in WiSE.<sup>8</sup> C 1s and O 1s spectra in Figure 3a detected strong signal between 289–290 and 531.5 eV ( $\text{Li}_2\text{CO}_3$  or alkylcarbonate) on the cycled  $\text{Mo}_6\text{S}_8$  electrode; however, with  $\text{Ar}^+$ -sputtering the abundance of  $\text{Li}_2\text{CO}_3$  decreases steadily (Figure 3b).  $\text{Li}_2\text{O}$ , on the contrary, increases (Figure 3c,d), suggesting an SEI of layered-structure, with  $\text{Li}_2\text{O}$  in the inner and  $\text{Li}_2\text{CO}_3$  in the



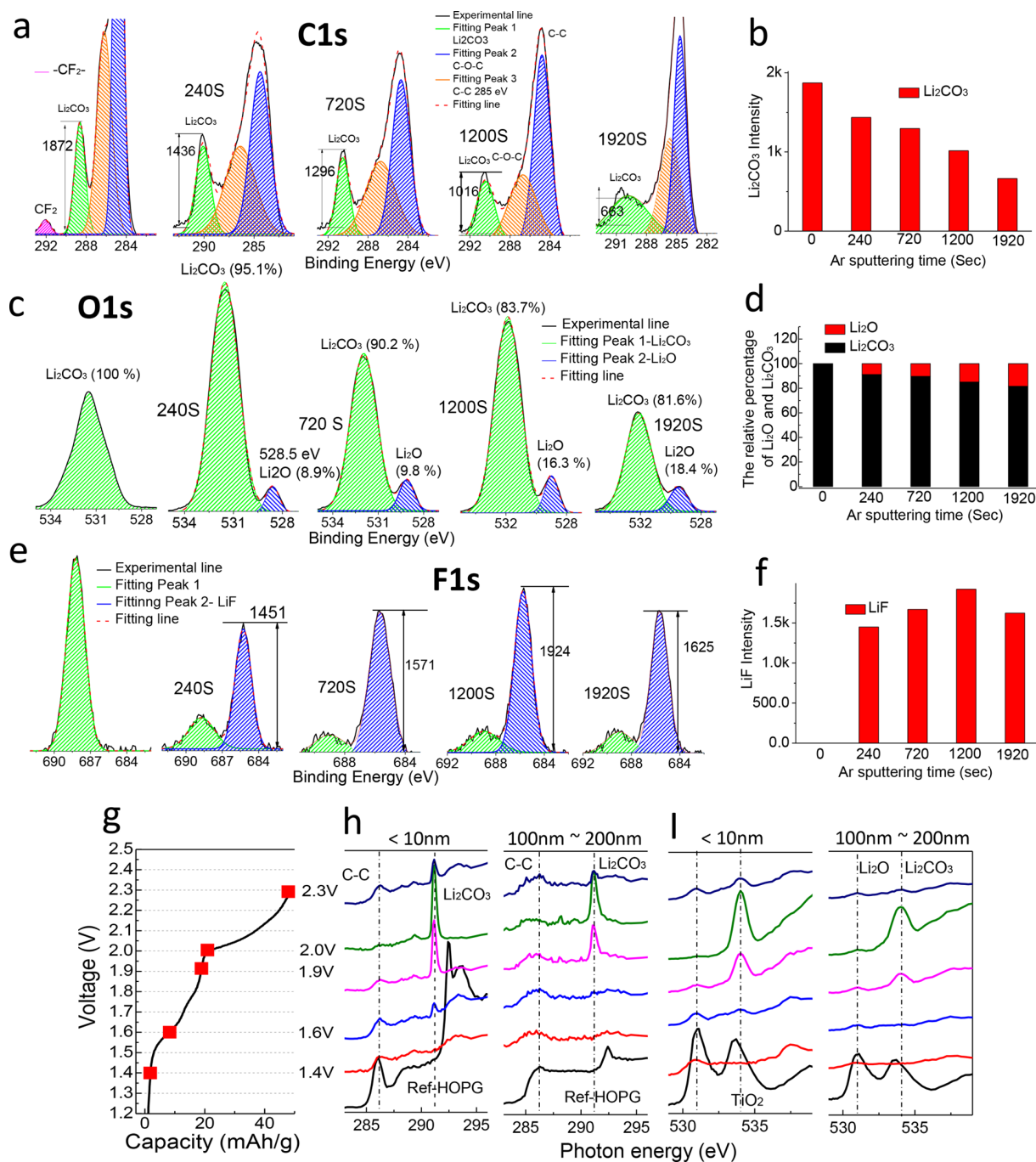


**Figure 3.** X-ray Photoelectron Spectroscopy (XPS) conducted on fully charged  $\text{Mo}_6\text{S}_8$  with various  $\text{Ar}^+$ -sputtering intervals and Soft X-ray Absorption Spectroscopy (SXAS) on cycled  $\text{Mo}_6\text{S}_8$  at different state-of-charge (SOC) in both bulk-sensitive TFY and surface sensitive mode corresponding to two detected penetration depths of <10 nm and 100–200 nm, respectively. (a) C 1s spectra; (b) the intensity change of  $\text{Li}_2\text{CO}_3$  with various etching durations from (a); (c) O 1s spectra; (d) the relative intensity of  $\text{Li}_2\text{O}$  and  $\text{Li}_2\text{CO}_3$  with the various etching durations of (c); (e) F 1s spectra; (f) the relative intensity of C–F and LiF with the various etching durations of (e); (g) the charge profile of full cell (LiMn<sub>2</sub>O<sub>4</sub>/Mo<sub>6</sub>S<sub>8</sub>); (h) C K-edge sXAS spectra at different SOC (1.4, 1.6, 1.9, 2.0 and 2.3 V) with highly oriented pyrolytic graphite (HOPG) as the reference; (i) O K-edge sXAS spectra at different SOC (1.4, 1.6, 1.9, 2.0 and 2.3 V) with TiO<sub>2</sub> as the reference.

outer layers, respectively. C and O K-edge SXAS spectra not only confirmed the existence of both  $\text{Li}_2\text{CO}_3$  and  $\text{Li}_2\text{O}$  in SEI, but also further verify that their formation occurs above 1.6 V of LiMn<sub>2</sub>O<sub>4</sub>/Mo<sub>6</sub>S<sub>8</sub> cell (Figure 3g,h,i). With increasing charge voltage, the intensity of  $\text{Li}_2\text{CO}_3$  and  $\text{Li}_2\text{O}$  signal gradually became stronger, no matter in deep (100–200 nm) or shallow (<10 nm) local regions. The only exception is the fully

charged electrode (2.3 V, SOC 100%), whose intensity is significantly lower due to the damage from water decomposition, because SEI has not been completely formed in this first cycle. Thus, it again indicated that SEI formation process has to compete with H<sub>2</sub> evolution, and its protection of the electrode against water decomposition would need certain

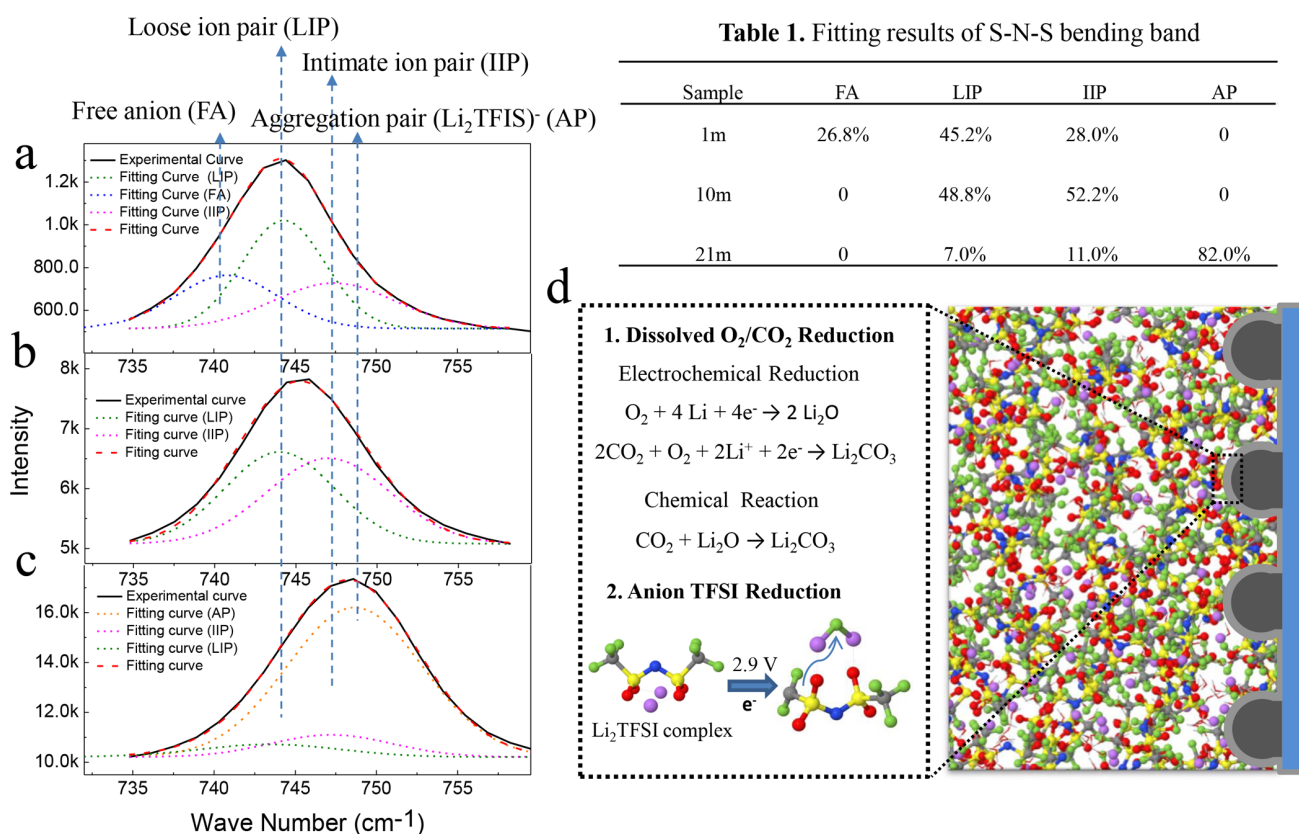


**Figure 4.** Raman spectra of  $\text{LiTFSI-H}_2\text{O}$  electrolytes ((a) 1 m, (b) 10 m, (c) 21 m) and its corresponding cation–anion coordination structure (Table 1) (Free anion (FA), Loose ion pair (LIP), Intimate ion pair (IIP) and Aggregation pair (AIG)). (d) SEI formation mechanisms in Water-in-Salt electrolyte.

number of cycles to take full effect. After 16 cycles,  $\text{Li}_2\text{CO}_3$  could be clearly detected at 100% SOC (2.3 V, Figure S5).

XPS confirmed the presence of F (Figure 3e), which came from two different sources: TFSI from the residual lithium salt or its partially fragmented form, as evidenced by F 1s at  $\sim 689$  eV (C–F species), and simple fluoride as evidenced by F 1s at 685–686 eV ( $\text{F}^-$ ). The latter will only be revealed after etched by  $\text{Ar}^+$  or  $\text{Ga}^{3+}$ , respectively. Apparently, TFSI reduction occurs at locations near the anode surface, leading to an SEI structure with the more completely reduced species reside in the inner region, such as simple inorganic salts  $\text{LiF}$  and  $\text{Li}_2\text{O}$ . This layered-structure is quite similar to SEIs formed in nonaqueous electrolytes.<sup>21,22</sup> With F and O apparently coming from the reduction of TFSI and water, the presence of  $\text{Li}_2\text{CO}_3$  may appear puzzling as there seems to be neither source of C (such as organic carbonate ester in nonaqueous electrolytes) nor mechanism to form O=C=O species (electrochemical oxidation of carbonaceous materials from composite electrodes is essentially impossible due to the prohibitively high energy barriers). We attributed its formation to the dissolved  $\text{CO}_2$  from the ambient, as all electrolyte preparation and cell assembly were conducted in ambient atmosphere. The slight acidic nature of WiSE (pH = 6.5–6.8)<sup>8</sup> confirms this hypothesis, as  $\text{LiTFSI}$  should render the aqueous solution slightly basic (pH > 7) when prepared under degassed conditions.

**2. Formation Mechanism of Aqueous SEI.** The chemical composition of SEI implies that two possible pathways contribute to its formation process: (1) reduction

of anion complexes or clusters; and (2) reduction of  $\text{O}_2$  and  $\text{CO}_2$  dissolved in the electrolyte (Figure 4d). The former provides the source for  $\text{LiF}$  and the latter for both  $\text{Li}_2\text{CO}_3$  and  $\text{Li}_2\text{O}$ . Both reactions are under heavy influence of the salt concentration. Raman spectra reveals intensified cation–anion interactions as salt concentration increases (Figure 4a), in which S–N–S bending peak shifts evidently from  $744 \text{ cm}^{-1}$  (1 m) to higher wavenumber at  $748 \text{ cm}^{-1}$  (21 m), because of the drastic change in cation ( $\text{Li}^+$ ) and anion ( $\text{TFSI}^-$ ) solvation structures and the corresponding electron density distributions on the TFSI. According to Li–TFSI distance,<sup>23</sup> the cation–anion clusters could be classified into free anion (FA)-( $\#\text{Li}^+ = 0$ )- $740 \text{ cm}^{-1}$ , loose ion pair (LIP)-( $\#\text{Li}^+ = 1$ )- $744 \text{ cm}^{-1}$ , intimate ion pair (IIP)-( $\#\text{Li}^+ = 1$ )- $747 \text{ cm}^{-1}$  and aggregate ion pair (AGP)-( $\#\text{Li}^+ = 2$ )- $748 \text{ cm}^{-1}$ , respectively, according to fitted Raman spectra (Figure 4a–c). The specific proportion of these four cation–anion coordination structures is listed in Table 1 (see Figure 4), which is found in good agreement with the analysis of Fourier-transformed infrared (FTIR) measurements and MD simulations for 10m and 21m.<sup>24</sup> In WiSE (21m), the percentage of AGP is  $\sim 82\%$ . As our previous MD simulation showed,<sup>8,24</sup> there is no sufficient water molecules at this high salt concentration to fully solvate all  $\text{Li}^+$  and separate them from TFSI. Instead,  $\text{Li}^+$  is coordinated by slightly less than two oxygens from TFSI, and slightly more than two oxygens from water. In such extended aggregates,  $\text{TFSI}^-$  is often shared by two or three  $\text{Li}^+$ .<sup>24</sup> Multiple  $\text{Li}^+$  coordination by the  $\text{TFSI}^-$  anions stabilized the transferred electron during reduction resulting in higher reduction potential. Earlier

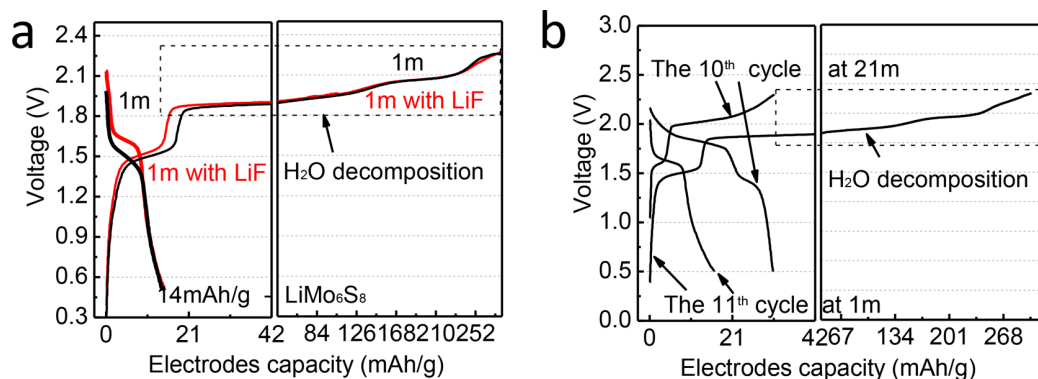
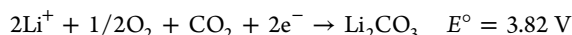
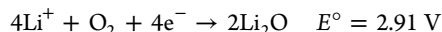


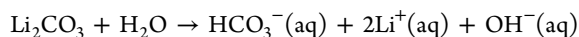
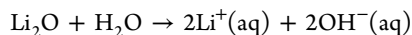
**Figure 5.** Solubility of aqueous SEI and the related electrochemical performance of aqueous Li-ion  $\text{LiMn}_2\text{O}_4/\text{Mo}_6\text{S}_8$  full cell: (a) in 1 m LiTFSI/ $\text{H}_2\text{O}$  with or without being saturated with LiF; (b) the same cell in 1 m LiTFSI/ $\text{H}_2\text{O}$  after an SEI was preformed in WiSE (21 m) for 10 cycles.

quantum chemistry study of the reduction reaction has identified  $\text{Li}_2(\text{TFSI})^+$  (Figure 3b) as the representative of highly aggregated ion aggregates in WiSE that would be reduced at the highest potential of 2.9 V, which might provide the essential basis for a SEI formation mechanism that could compete with water reduction.

On the other hand, in  $\text{Li}^+$ -conducting electrolytes, the theoretical reduction potentials of most dissolved gases ( $\text{O}_2$  and  $\text{CO}_2$ ) usually situate at higher values:



In diluted aqueous electrolytes, these gaseous solute never gets the opportunity of forming solid deposits on electrode surfaces as their reduction products would quickly hydrolyze and dissolve:



Thus, the scenario of an SEI consisting of  $\text{Li}_2\text{CO}_3$  and  $\text{Li}_2\text{O}$  would be beyond possibilities in diluted aqueous solutions. It was the superconcentration of LiTFSI in WiSE that makes it possible for LiF,  $\text{Li}_2\text{CO}_3$  and  $\text{Li}_2\text{O}$  to deposit on anode surface without dissolution. Simultaneously, the superconcentration also results in a significant depletion of free water fraction in WiSE (15% at 21 m LiTFSI). Hence, much fewer water molecules are available to be adsorbed on the electrode surface, which is often the first step of water decomposition reactions. Moreover, in the highly concentrated LiTFSI-based electrolytes the  $\text{CF}_3$ -groups of TFSI<sup>-</sup> anions tend to preferentially adsorb at the negative electrode surfaces potentials above 2.5 V vs Li/Li<sup>+</sup>. This preferential adsorption further facilitates LiF formation.<sup>25</sup> The fortuitous combination of all these factors leads to the formation of a composite SEI that consists of LiF,  $\text{Li}_2\text{CO}_3$  and  $\text{Li}_2\text{O}$ , with LiF being the dominant ingredient.

### 3. Solubility and Continuous Growth of Aqueous SEI.

To support reversible cell reactions, SEI must remain stable in the bulk electrolyte against both electrochemical reactions and chemical dissolution. Given that water is one of the most powerful solvents, as characterized by its high dielectric constant, dipole moment and acceptance/donor numbers, an aqueous SEI faces much more severe challenges than its nonaqueous counterpart does. LiF-rich SEI cannot form on

$\text{Mo}_6\text{S}_8$  anode in 1 m LiTFSI electrolyte, as the  $\text{Mo}_6\text{S}_8$  anode mainly induces water reduction reaction rather than lithiation, as demonstrated by the low discharge capacity and low Coulombic efficiency in Figure 5a. This is because the sustained hydrogen evolution occurs at higher or similar potential as the TFSI reduction, preventing LiF deposition in dense form and the subsequent constitution of a passivation layer. In addition, the SEI components also suffer higher solubility in a dilute aqueous solution, which further increases the difficulty in building up a robust SEI. For example, even the least soluble lithium salt, LiF, remains slightly soluble in neat water (about 0.04 mol/L),<sup>26</sup> which is high enough to disrupt an SEI based on LiF in the dilute electrolytes considering the nanometric existence of interphase. This constitutes the main reason why a  $\text{LiMn}_2\text{O}_4/\text{Mo}_6\text{S}_8$  full cell cannot charge/discharge in 1 m LiTFSI, even after an effective SEI was preformed on  $\text{Mo}_6\text{S}_8$  anode in WiSE. In this scenario, the preformed SEI consisting of LiF,  $\text{Li}_2\text{CO}_3$  and  $\text{Li}_2\text{O}$  obviously falls apart by dissolving in the dilute electrolyte (Figure 5b). Thus, superconcentration is not only required for the formation process of SEI, but also necessary to maintain and repair such an aqueous SEI. On the other hand, the excellent cycling stability of various battery chemistries demonstrated in WiSE implies that the aqueous SEI formed in WiSE must be highly resistant to the dissolution by the water molecules therein.<sup>8–13</sup> Here the “Common Ion Effect” exerts by the extremely high  $\text{Li}^+$ -population in WiSE is a critical prerequisite for keeping these inorganic lithium salts in solid form and maintain the composite SEI.

Even in the best nonaqueous electrolyte, the continuous growth of formed SEI is inevitable, as indicated by the parasitic processes revealed by the high precision Coulometric studies.<sup>27,28</sup> The instability of SEI can also be reflected in the long term storage and self-discharge experiments. As Dahn and co-workers taught, an electrolyte or the durability of an SEI would experience the most rigorous test when it is exposed to extreme potentials.<sup>25</sup> To understand how robust the aqueous SEI is, the decay of open circuit voltages (OCV) were monitored for a series of fully charged aqueous Li-ion cells. As Figure 6 shows, the OCV significantly stabilizes if the SEI was formed either at a low rate of 0.1 C (Figure 6a), or after extended cycling at 1 C (Figure 6b). These results basically manifest that the integrity of SEI is only dependent on the duration of time that the electrolyte spent at the forming potentials. The best quality of SEI was obtained within 10 cycles at 1 C, as demonstrate by the stable potential



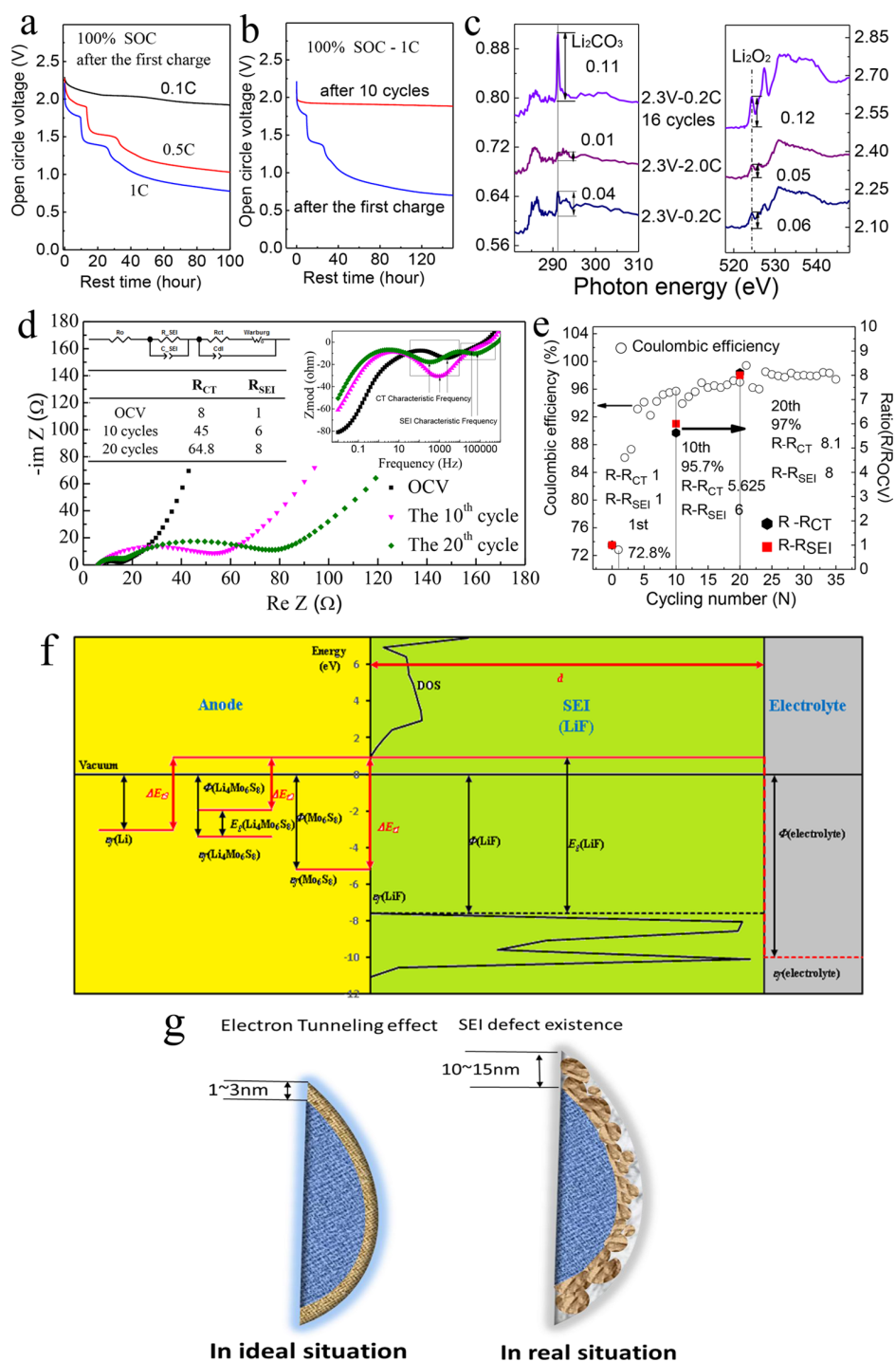


**Figure 6.** The stability of aqueous SEI. (a,b) Open circuit potentials (OCV) decays with rest time. (a) the cell is first fully charged to 2.3 V at different rate (C/5, C/2 and C), then rest at 100% Stage of Charge (SOC); (b) the cells are rested at 100% SOC after different cycles at high rate (1C). (c) C and O K-edge SXAS spectra of the aqueous SEI formed on  $\text{Mo}_6\text{S}_8$  at different cycles (1 and 16 cycles) and rates (0.2 and 2 C) in the surface-sensitive TEY mode with the detected penetration depth of <math>< 10\text{ nm}</math>. (d,e) Electrochemical Impedance Spectrum (EIS) at different cycles (full-cell after 24 h resting, 10 cycles and 20 cycles). (d) Nyquist plots with the inset of Bode plots and equivalent circuit fitting based on ESI experimental data; (e) the corresponding Coulombic efficiency. (f) Scheme of the ideal and actual SEI formations: (i) ideal SEI formation dependent on electron tunneling effect, (ii) actual SEI formation taking into account the atomic defect, grain boundary and inhomogeneous growth. (g) Calculation of electron tunneling barrier ( $\Delta E_t$ ) by aligning the Fermi level ( $e_f$ ), work function ( $\Phi$ ) and band gap ( $E_g$ ) of the lithium anode and SEI.

without any evident drop for 150 h. C and O K-edge sXAS spectra of cycled  $\text{Mo}_6\text{S}_8$  lead to the same conclusion, where the intensities for both  $\text{Li}_2\text{CO}_3$  and  $\text{Li}_2\text{O}$  reach high level only

after multiple (16) cycles (Figure 6c) or at low (0.2 C) charging rate (Figure S5).



In actual battery environments, the formation process of SEI is rather complicated, which is difficult to be described by a simple equation. Here we adopted the model of diffusion-limitation for the growth of nonaqueous SEIs:<sup>27,29</sup>

$$\frac{dx}{dt} = \sqrt{\frac{\kappa}{2}} t^{-1/2} \quad (1)$$

where  $\kappa$  is a constant dependent on electrolyte/electrode and temperature,  $t$  is time,  $x$  is the hypothetical thickness of an idealized SEI, and  $dx/dt$  is SEI growing rate.

A few assumptions were made here: (1) SEI component is homogeneous and unchanged with SEI layer thickness ( $x$ ), (2) SEI is uniform without any defects like cracks or holes. Based on above oversimplifications (most of which are almost certainly not true but nevertheless provide a good-enough approximation), we measured electrochemical impedance spectra at different cycles (Figure 6d). Nyquist and Bode plots at OCV stage showed only one semicircle in medium frequency ( $\sim 2400$  Hz) corresponding to charge-transfer resistance ( $R_{ct}$ ), while no response from SEI component occurs in resting process. Once the cell has been cycled 10 cycles, a new semicircle appears in high frequency range ( $\sim 10^5$  Hz), which was assigned to SEI.<sup>5,30</sup> This semicircle becomes more obvious after 20 cycles, indicating its full formation. The fitted results using an equivalent circuit (Figure 6d inset) show that the resistance of SEI ( $R_{SEI}$ ) also increases with the cycling, with Coulombic efficiency gradually approaching 100%. In order to exclude any interference from the cathode side, the EIS of the anode was also collected in three-electrode device after the initial 2 formation cycles (Figure S6).

Among the many models and theories to predict SEI thickness, electron tunneling model (ETM) proposed by Peled is widely accepted, which states that SEI thickness is determined by the electron tunneling range.<sup>31</sup> DFT calculations were employed to predict the electronic tunneling barriers and SEI thickness.<sup>32</sup> Figure 6e shows the energy levels of anode materials (such as Li,  $\text{Mo}_6\text{S}_8$  and  $\text{Li}_4\text{Mo}_6\text{S}_8$ ), SEI component (such as LiF), and electrolyte, as highlighted in yellow, green and gray, respectively. The DFT computed relative position of the Fermi level ( $\epsilon_f$ ), band gaps ( $E_g$ ), and work function ( $\Phi$ ) of each material, together with the density of states (DOS) around the band gap of LiF, are aligned with respect to a common reference, the vacuum, which is set as 0 eV for a better comparison. Therefore, if any excess electron from the electronic conducting electrode tunnels through the electronic insulating SEI component to reach electrolyte, it has to overcome the electronic tunneling energy barrier ( $\Delta E_t$ ) from the Fermi level ( $\epsilon_f$ ) of anode material to the bottom of the conduction band of SEI component. According to Figure 6f, the electronic tunneling energy barrier can be calculated, as shown in eq 2, and the electronic tunneling probability is assumed as shown in eq 3 to a very small value of  $e^{-40}$ :

$$\Delta E_t = E_g(\text{SEI}) - \Phi(\text{SEI}) + \Phi(\text{anode}) - E_g(\text{anode}) \quad (2)$$

$$T = \frac{16\epsilon_f\Delta E_t}{(\epsilon_f + \Delta E_t)^2} e^{-4\pi d/h\sqrt{2m\Delta E_t}} \quad (3)$$

The critical thickness of SEI,  $d^*$ , that blocks electron tunneling can thus be estimated. Actually, if we assume that SEI layer component is only composed by a single crystal insulating LiF while ignoring any defect and grain boundary, its thickness

under this ideal condition can be determined (Figure 6g). The computed electron tunneling barrier and the thickness of SEI layer for both unlithiated  $\text{Mo}_6\text{S}_8$  and full lithiated  $\text{Li}_4\text{Mo}_6\text{S}_8$  are summarized in Table S1. The former behaves as a metallic conductor, on which the critical SEI thickness is  $\sim 1.6$  nm for LiF. However, the latter  $\text{Li}_4\text{Mo}_6\text{S}_8$  became an insulator with band gap of 1.46 eV, which will significantly decrease the electronic tunneling barrier and increase the critical SEI thickness to  $\sim 2.4$  nm. Experimentally, we have observed using high solution TEM that SEI thickness ranges between 10 and 15 nm, similar to nonaqueous SEIs observed previously (Figure 6g). We believe that the above difference can probably be ascribed to the following factors. (1) SEI in real life is composed not only by LiF but also  $\text{Li}_2\text{O}$  and  $\text{Li}_2\text{CO}_3$  (Figure 2 and 3), among which pure LiF has the largest tunneling barrier, thus the mixture of which is expected to have increased SEI critical thickness;<sup>32</sup> (2) The significant mismatch in the lattice parameter between  $\text{Mo}_6\text{S}_8$  and LiF inevitably induces tension in SEI, which further intensifies with the volume expansion of  $\text{Mo}_6\text{S}_8$  after lithiation. This will also decrease the band gap of LiF and increase the critical thickness of SEI;<sup>32</sup> (3) Inhomogeneous SEI formation process including grain boundary, cationic and anionic defects and multicomponents, which makes SEI far from being perfectly dense; and (4) other potential electron transport mechanisms may also be involved, resulting from the formation of defects and polarons. These effects make it possible for an electron to tunnel not just once (“ballistic”), but multiple times, giving rise to more diffusive hopping transport behavior. As the SEI grows thicker, it might be necessary for species like  $\text{Li}_2(\text{TFSI})^+$  to partly penetrate the SEI through diffusion, before meeting the electron and get reduced. These diffusive mechanisms underline the parabolic kinetic law (2), when  $x$  has grown thick enough. When  $x$  is ultrathin and single-tunneling is sufficient, the Cabrera-Mott regime growth law is more appropriate.

On the basis of the above results, we now can envision a comprehensive picture of how an aqueous SEI forms in aqueous electrolytes. In the superconcentrated (21 m) solution of LiTFSI in water, extensive ionic cluster forms due to the limited availability of water molecules. The intimate interaction between cation and anion leads to two consequences: (1) the activity of water molecule is so suppressed that the electrolyte becomes rather resistant against oxidation at cathode surface, and (2) the reduction potential of TFSI in the ionic clusters is significantly raised to levels competitive with  $\text{H}_2$  evolution.

During the SEI formation, there are actually three sources contributing to the irreversible reduction reactions: (1) dissolved  $\text{O}_2$  and  $\text{CO}_2$ , (2) salt anion and (3) water molecule. Among them, water decomposition is purely parasitic because it does not contribute to SEI component while depleting lithium source. The competition among these irreversible reactions would determine whether an SEI can be formed or how stable it is against dissolution by aqueous electrolytes. The formation of aqueous SEI might experience a few distinct stages:

- (1) The reductions of dissolved gas and TFSI (between 1.9–2.90 V), where the electrode potential still sits comfortably within the electrochemical stability window of the electrolyte. The reduction products are expected to adhere to the electrode surface, but the formation of complete SEI needs long time (i.e., few cycles in galvanostatic charge/discharge cycles). When the

electrode sits at a low potential long enough, the final reduction products (LiF, Li<sub>2</sub>O and Li<sub>2</sub>CO<sub>3</sub> start to form. The insolubility of these simple inorganic salts in WiSE provides better adhesion to anode surface, thus effectively shielding the anode surface and prevented further H<sub>2</sub>-evolution. It is during this stage that robust and protective SEI come into shape, although it will take more than one cycle to consolidate its chemical and mechanical durability.

- (2) The coexistence of all irreversible reactions (<1.9 V), where the reduction of water starts with H<sub>2</sub>-evolution. H<sub>2</sub> gas bubbling, even at nanoscale, would pose significant erosion risk. This reaction competes with the reduction of dissolved gas and TFSI, and interferes the adhesion of their products to the anode surface.
- (3) It should be kept in mind that, even during the long-term cycling and storage after SEI is formed, SEI still faces the sustained dissolution, corrosion, cracking and reforming, and the presence of superconcentrated electrolyte is essential to repair and maintain such an aqueous SEI.

## CONCLUSION

In this work we rigorously characterized the chemistry, microstructure, formation mechanism and stability/durability of a new SEI formed in aqueous electrolyte. Using a combination of in situ/ex situ spectra techniques, we analyzed its exact chemical compositions, and demonstrated how reductive decompositions of TFSI, dissolved O<sub>2</sub> and CO<sub>2</sub>, and water molecule compete in the very first formation process. Several key factors responsible for the successful formation of aqueous SEI were identified, which include the salt concentration, chemical structure of salt anion, possible reduction products and their solubilities in aqueous electrolyte, and the formation condition. A model for the durability and aging of aqueous SEI was also proposed. This molecular-level understanding about this new interphasial chemistry establishes a guiding principle to tailor-design of better aqueous SEI that helps to eventually resolve the “cathodic challenge” in high-voltage aqueous batteries.

## EXPERIMENTAL SECTION

Lithium bis(trifluoromethane sulfonyl) imide (LiN(SO<sub>2</sub>CF<sub>3</sub>)<sub>2</sub>, LiTFSI) (>98%, TCI) and water (HPLC grade, Sigma-Aldrich) were used as received. Aqueous electrolytes are prepared according to molality (mol-salt in kg-solvent), which were coded by abbreviated concentrations (1 m, 5 m, 10 m, 21 m), with LiTFSI molar fractions being 0.0177 (1m), 0.0826 (5m), 0.1526 (10 m) and 0.2743 (21 m), respectively. The preparation of chevrel phase Mo<sub>6</sub>S<sub>8</sub> was described previously, while LiMn<sub>2</sub>O<sub>4</sub> was purchased from MTI Corporation. Composite electrodes were fabricated by compressing active materials, carbon black, and poly(vinylidene difluoride) (PTFE) at a weight ratio of 8:1:1 onto a stainless steel grid. The full aqueous Li-ion cell was assembled in CR2032-type coin cell using LiMn<sub>2</sub>O<sub>4</sub> cathode, Mo<sub>6</sub>S<sub>8</sub> anode and glass fiber as separator. The cells were cycled galvanostatically on a Land BT2000 battery test system (Wuhan, China). Electrochemical impedance spectroscopy (EIS) was measured on Gamry Interface 1000 (Gamry, USA).

The gas evolution during the formation stage of SEI was quantitatively analyzed with differential electrochemical mass spectrometry (DEMS) and custom-built gastight Swagelok cells, in which anode (Mo<sub>6</sub>S<sub>8</sub>), separator, cathode (LiMn<sub>2</sub>O<sub>4</sub>), a stainless steel ring spacer (1 mm in height) and 65 μL of aqueous electrolytes at varying LiTFSI-concentrations were sequentially added. The cell structures and DEMS operation mechanisms have been described

previously.<sup>17</sup> To ensure that only the gas generated from the electrochemical reaction be detected, the cells were purged with Ar (~1120 Torr, Research Purity, Matheson Tri-Gas) overnight, so that any residual gas, either dissolved in electrolytes or adsorbed in cell components, was completely removed. To minimize any possible water transfer to mass spectrometry, a cold trap was installed at the cell outlet capillaries.

Chemical analysis and depth-profiling of SEI was conducted using time-of-flight secondary ion mass spectrometry (TOF-SIMS), which is attached on a GAIA Focused Ion Beam and Scanning Electron Microscope. This unique integration of ion mass spectrometry of high sensitivity together with continual FIB etching/sectioning results in a 3D map of mass distribution across the SEI. The depth profiling experiments were performed in static mode where the sputtering gun (Ga<sup>+</sup>) was operated over a 4 × 4 μm<sup>2</sup> area of the electrode surface. Secondary ions were detected in both positive and negative ion mode. TOF-SIMS spectra data were deconvoluted using proprietary TOF-SIMS explorer software.

X-ray photoelectron spectroscopy (XPS) analysis was performed with a high resolution Kratos AXIS 165 X-ray photoelectron spectrometer using monochromic AlKα radiation. All samples were recovered from full aqueous Li-ion cells in 2032 coin cell configuration after repeated cycling to complete SEI formation. The samples were washed by dimethoxyethane (DME) for three times and then dried under vacuum for 2 h before entry into XPS chamber. Raman spectra were acquired using Horiba Jobin Yvon Labram Aramis by a 532 nm diode-pumped solid-state laser between 1200 and 100 cm<sup>-1</sup>. Laser power was set at 150–450 mW, and 400 scans were accumulated with a resolution of 2 cm<sup>-1</sup>. All samples were sealed in a test glass tube.

Soft X-ray Absorption Spectroscopy (SXAS) measurements of C, O and F K-edges were performed at beamline 8.0. One of the Advance Light Source (ALS) of Lawrence Berkeley National Laboratory (LBNL). The undulator and spherical grating monochromator supply a linearly polarized photon beam with resolving power up to 6000. The energy resolution of sXAS is higher than 0.15 eV in this study. All experiments were performed at room temperature, and all spectra were normalized to the beam flux measured by an upstream gold mesh, which is cleaned through in-vacuum Au evaporation especially for C- K and O- K sXAS experiments.

## ASSOCIATED CONTENT

### Supporting Information

The Supporting Information is available free of charge on the ACS Publications website at DOI: 10.1021/jacs.7b10688.

Figures S1–S6; Table S1 (PDF)

## AUTHOR INFORMATION

### Corresponding Authors

\*liju@mit.edu  
\*conrad.k.xu.civ@mail.mil  
\*cswang@umd.edu

### ORCID

Dahyun Oh: 0000-0003-1390-8440  
Oleg Borodin: 0000-0002-9428-5291  
Yue Qi: 0000-0001-5331-1193  
Wanli Yang: 0000-0003-0666-8063  
Feng Pan: 0000-0002-8216-1339  
Ju Li: 0000-0002-7841-8058  
Chunsheng Wang: 0000-0002-8626-6381

### Notes

The authors declare no competing financial interest.

## ■ ACKNOWLEDGMENTS

CW and KX acknowledge support from DOE ARPA-E (DEAR0000389). LMS acknowledges support from One Hundred Talents Program of the Chinese Academy of Sciences. YXL, YQ, and CSW acknowledge the support for the computational work as part of the Nanostructures for Electrical Energy Storage (NEES), an Energy Frontier Research Center funded by the U.S. Department of Energy, Office of Science, Basic Energy Sciences under Award Number DESC0001160. JL acknowledges support by NSF ECCS-1610806. This research used resources of the Advanced Light Source, which is a DOE Office of Science User Facility under Contract No. DE-AC02-05CH11231.

## ■ REFERENCES

- (1) Fong, R.; Vonsacken, U.; Dahn, J. R. *J. Electrochem. Soc.* **1990**, *137*, 2009.
- (2) Xu, K. *Chem. Rev.* **2004**, *104*, 4303.
- (3) Xu, K. *Chem. Rev.* **2014**, *114*, 11503.
- (4) Xu, K.; Lam, Y. F.; Zhang, S. S.; Jow, T. R.; Curtis, T. B. *J. Phys. Chem. C* **2007**, *111*, 7411.
- (5) Levi, M. D.; Aurbach, D. *J. Phys. Chem. B* **1997**, *101*, 4630.
- (6) Besenhard, J. O.; Winter, M.; Yang, J.; Biberacher, W. *J. Power Sources* **1995**, *54*, 228.
- (7) Tasaki, K.; Kanda, K.; Kobayashi, T.; Nakamura, S.; Ue, M. *J. Electrochem. Soc.* **2006**, *153*, A2192.
- (8) Suo, L.; Borodin, O.; Gao, T.; Olguin, M.; Ho, J.; Fan, X.; Luo, C.; Wang, C.; Xu, K. *Science* **2015**, *350*, 938.
- (9) Suo, L. M.; Borodin, O.; Sun, W.; Fan, X. L.; Yang, C. Y.; Wang, F.; Gao, T.; Ma, Z. H.; Schroeder, M.; von Cresce, A.; Russell, S. M.; Armand, M.; Angell, A.; Xu, K.; Wang, C. S. *Angew. Chem., Int. Ed.* **2016**, *55*, 7136.
- (10) Yang, C. Y.; Suo, L. M.; Borodin, O.; Wang, F.; Sun, W.; Gao, T.; Fan, X. L.; Hou, S. Y.; Ma, Z. H.; Amine, K.; Xu, K.; Wang, C. S. *Proc. Natl. Acad. Sci. U. S. A.* **2017**, *114*, 6197.
- (11) Suo, L. M.; Han, F. D.; Fan, X. L.; Liu, H. L.; Xu, K.; Wang, C. S. *J. Mater. Chem. A* **2016**, *4*, 6639.
- (12) Suo, L.; Borodin, O.; Wang, Y.; Rong, X.; Sun, W.; Fan, X.; Xu, S.; Schroeder, M. A.; Cresce, A. V.; Wang, F.; Yang, C.; Hu, Y.-S.; Xu, K.; Wang, C. *Advanced Energy Materials* **2017**, *7*, 1701189.
- (13) Yang, C.; Chen, J.; Qing, T.; Fan, X.; Sun, W.; von Cresce, A.; Ding, M. S.; Borodin, O.; Vatamanu, J.; Schroeder, M. A.; Eidson, N.; Wang, C.; Xu, K. *Joule* **2017**, *1*, 122.
- (14) Kim, H.; Hong, J.; Park, K. Y.; Kim, H.; Kim, S. W.; Kang, K. *Chem. Rev.* **2014**, *114*, 11788.
- (15) Luo, J. Y.; Cui, W. J.; He, P.; Xia, Y. Y. *Nat. Chem.* **2010**, *2*, 760.
- (16) Li, W.; Dahn, J. R.; Wainwright, D. S. *Science* **1994**, *264*, 1115.
- (17) McCloskey, B. D.; Bethune, D. S.; Shelby, R. M.; Girishkumar, G.; Luntz, A. C. *J. Phys. Chem. Lett.* **2011**, *2*, 1161.
- (18) Xu, K.; Wang, C. *Nat. Energy* **2016**, *1*, 16161.
- (19) Fisher, G. L.; Ohlhausen, J. A.; Wetteland, C. J. *Surf. Interface Anal.* **2005**, *37*, 713.
- (20) Wilson, D. J.; Williams, R. L.; Pond, R. C. *Surf. Interface Anal.* **2001**, *31*, 385.
- (21) von Cresce, A.; Russell, S. M.; Baker, D. R.; Gaskell, K. J.; Xu, K. *Nano Lett.* **2014**, *14*, 1405.
- (22) Lu, P.; Harris, S. J. *Electrochem. Commun.* **2011**, *13*, 1035.
- (23) McOwen, D. W.; Seo, D. M.; Borodin, O.; Vatamanu, J.; Boyle, P. D.; Henderson, W. A. *Energy Environ. Sci.* **2014**, *7*, 416.
- (24) Borodin, O.; Suo, L.; Gobet, M.; Ren, X.; Wang, F.; Faraone, A.; Peng, J.; Olguin, M.; Schroeder, M.; Ding, M. S.; Gobrogge, E.; von Wald Cresce, A.; Munoz, S.; Dura, J. A.; Greenbaum, S.; Wang, C.; Xu, K. *ACS Nano* **2017**, *11*, 10462.
- (25) Vatamanu, J.; Borodin, O. *J. Phys. Chem. Lett.* **2017**, *8*, 4362.
- (26) Jones, J.; Anouti, M.; Caillon-Caravanier, M.; Willmann, P.; Lemordant, D. *J. Mol. Liq.* **2010**, *153*, 146.
- (27) Smith, A. J.; Burns, J. C.; Zhao, X. M.; Xiong, D. J.; Dahn, J. R. *J. Electrochem. Soc.* **2011**, *158*, A447.
- (28) Smith, A. J.; Burns, J. C.; Dahn, J. R. *Electrochem. Solid-State Lett.* **2010**, *13*, A177.
- (29) Ploehn, H. J.; Ramadass, P.; White, R. E. *J. Electrochem. Soc.* **2004**, *151*, A456.
- (30) Thomas, M.; Bruce, P. G.; Goodenough, J. B. *J. Electrochem. Soc.* **1985**, *132*, 1521.
- (31) Peled, E. *J. Electrochem. Soc.* **1979**, *126*, 2047.
- (32) Lin, Y. X.; Liu, Z.; Leung, K.; Chen, L. Q.; Lu, P.; Qi, Y. J. *Power Sources* **2016**, *309*, 221.